GASP – XIX. AGN and their outflows at the centre of jellyfish galaxies

Mario Radovich [1][*] Bianca Poggianti,[1] Yara L. Jaffé [2] Alessia Moretti [1]
Daniela Bettoni,[1] Marco Gullieuszik,[1] Benedetta Vulcani [1] and Jacopo Fritz [3]

[1]*INAF- Osservatorio astronomico di Padova, Vicolo Osservatorio 5, I-35122 Padova, Italy*
[2]*Instituto de Física y Astronomía, Facultad de Ciencias, Universidad de Valparaíso, Avda. Gran Bretaña 1111, Casilla 5030, Valparaíso, Chile*
[3]*Instituto de Radioastronomía y Astrofísica, UNAM, Campus Morelia, A.P. 3-72, C.P. 58089, Mexico*

ABSTRACT

The GASP survey, based on MUSE data, is unveiling the properties of the gas in the so-called
'jellyfish' galaxies: these are cluster galaxies with spectacular evidence of gas stripping by ram
pressure. In a previous paper (Poggianti et al.), we selected the seven GASP galaxies with the
most extended tentacles of ionized gas, and based on individual diagnostic diagrams concluded
that at least five of them present clear evidence for an active galactic nucleus. Here we present
a more detailed analysis of the emission lines properties in these galaxies. Our comparison of
several emission line ratios with both AGN and shock models show that photoionization by the
AGN is the dominant ionization mechanism. This conclusion is strengthened by the analysis of
$H\beta$ luminosities, the presence of nuclear iron coronal lines, and extended (>10 kpc) emission
line regions ionized by the AGN in some of these galaxies. From emission line profiles, we
find the presence of outflows in four galaxies, and derive mass outflow rates, time-scales, and
kinetic energy of the outflows.

Key words: galaxies: active – galaxies: clusters: general.

1 INTRODUCTION

It is now widely accepted that there is a strong connection between
the presence of an active galactic nucleus (AGN) and the host galaxy
properties, based both on cosmological models and observational
results from wide-field surveys (see e.g. Heckman & Best 2014, and
refs for a review). However, the way this interaction occurs is still
unclear, and it may actually be the outcome of a wide range of differ-
ent physical processes (e.g. merging, bars). A major improvement
in our understanding of the complex environment around AGN
is given by the availability of Integral Field Spectroscopy (IFU),
allowing to map emission line fluxes and kinematics tracing the
AGN and its surroundings (see e.g. Venturi et al. 2018; Ilha et al.
2019; Mingozzi et al. 2019).

An important issue is the effect of the environment on the
presence of the AGN: it is still debated (see e.g. Marziani et al.
2017, and refs) whether or not a dense galaxy environment such
as in galaxy clusters has any effect on the presence of AGN.
Early spectroscopic studies (Dressler, Thompson & Shectman 1985)
suggested that the fraction of AGN in clusters (~1 per cent) is
significantly lower than in a field environment (~5 per cent). Later
studies based on X-ray data (Pimbblet et al. 2013) did not however
confirm this result, showing comparable fractions of AGN in cluster
and field, though there may be an effect related to distance from

the cluster centre (Ehlert et al. 2014). In this context, Marshall
et al. (2018) used semi-analytic galaxy evolution models to show
that both star formation and AGN can be triggered by the ram
pressure as they move through the intracluster medium, in galaxies
located at distances from the cluster centre larger than the virial
radius; at smaller distances, where the ram pressure is higher,
models suggest that the gas is stripped from the galaxy and cannot
feed the AGN. Ramos-Martínez, Gómez & Pérez-Villegas (2018)
analysed the role of the galactic magnetic field in the gas stripping
using 3D magnetohydrodynamic simulations: they found that the
magnetic field can contribute to generate a gas inflow to the central
parts of the galaxies, triggering star formation and maybe feeding
the AGN.

Conversely, the presence of the AGN may impact the surrounding
environment in many ways (see e.g. Fabian 2012, for a review): in
particular, they are able to drive outflows of ionized gas and impact
on the galaxy environment on scales that may range from few kpc
(see e.g. Bing et al. 2019) for the less luminous AGN to tens of kpc
for the brightest AGN (Harrison et al. 2014).

The *GAs Stripping Phenomena* (GASP) survey (Poggianti et al.
2017a, P17a hereafter) is aimed at studying with the MUSE Integral
Field spectrograph on VLT the properties of the so-called *jellyfish*
galaxies in clusters, whose *tentacles* of UV and optically bright
material that make them similar to a jellyfish (Smith et al. 2010) are
thought to originate via ram pressure stripping by the intracluster
medium (Ebeling, Stephenson & Edge 2014; Fumagalli et al. 2014;
Rawle et al. 2014; Fossati et al. 2016). Poggianti et al. (2017b;

* E-mail: mario.radovich@inaf.it

P17b hereafter) showed that at least five and possibly six of seven galaxies with the strongest evidence of gas stripping and the most favourable conditions for ram pressure (Jaffé et al. 2018) host an AGN, suggesting a connection between ram pressure stripping and AGN triggering. In P17b the [N II] λ6583/Hα versus [O III] λ5007/Hβ line ratios were used to select the most likely mechanism that ionized the gas: radiation from hot young stars in star-forming regions, from an AGN, a combination of them (*composite*), and either low-luminosity AGN or shocks (LINERs), using as reference the classification by Kewley et al. (2006). As already shown in Poggianti et al. (2019), adding other line ratio diagnostic diagrams such as [O I] λ6300/Hα and [S II] λλ6716, 6731/Hα versus [O III] λ5007/Hβ (Veilleux & Osterbrock 1987) can provide a more detailed description of the physical processes at work. In this paper we expand the work by P17b and critically scrutinize those results using all three main diagnostic diagrams simultaneously and comparing observed line ratios with photoionization and shock models. Moreover, we inspect additional features such as coronal Fe lines and analyse separately the extended extranuclear AGN-powered emission regions. Finally, we discuss the presence and properties of outflows.

The paper is structured as follows. A short summary of the data and how they were analysed is given in Section 2. In Section 3, observed emission line ratios are compared with both photoionization and shock models, to confirm that photoionization from the AGN is required to reproduce the line ratios and derive the best-fitting model parameters. As further probes of the AGN, we estimate the maximum contribute to the observed Hβ luminosity from shock models; in some cases, we detect the presence of high-ionization iron coronal lines (JO201 and JO135) and of extended (>10 kpc) AGN-like emission lines (JO204 and JO135): this is used in Section 3.4 to derive the number of ionizing photons that should be emitted by the AGN. In Section 4 we analyse the [O III] λ5007 line as a tracer of outflows around the AGN and derive their size, outflow rates, time-scales, and kinetic energy. Conclusions are given in Section 5.

The cosmology concordance model was adopted: $H_0 = 70$ km s^{-1} Mpc^{-1}, $\Omega_{\rm m} = 0.3$, $\Omega_\Lambda = 0.7$.

2 GALAXY SAMPLE, OBSERVATIONS, AND DATA ANALYSIS

In this paper we analyse the seven galaxies in P17b (Table 1 and Fig. 1), which are all characterized by tails of ionized gas at least as long as the stellar galaxy diameter. These galaxies represent extreme cases where the cluster environment strongly acts on the gas and possibly on the AGN. Spectra and individual emission lines for the central spaxel of each galaxy, selected as discussed later, are displayed in Fig. 2. In the following description, a reference is given after the galaxy name for those galaxies studied individually in a GASP paper.

JO201, or Kaz 364 (Bellhouse et al. 2017; P17a; George et al. 2018) was also classified by Arnold et al. (2009) as an AGN based on *XMM* observations. Two components are present in the nuclear emission lines (P17b, see also Fig. 2): a narrow, stronger component, and a broader one, slightly blueshifted.

JO204 (Gullieuszik et al. 2017) was included by Nevin et al. (2016) in a sample of 71 double-peaked AGN selected from the SDSS and classified as an AGN with an outflow. At least two components are visible in the MUSE spectra; an extended emission with AGN-like line ratios is detected up to ~20 kpc from the nucleus, see below Section 3.4.

JO135 Complex emission line profiles are observed in the nucleus, with a strong redshifted wing (Fig. 2). AGN-like emission is present up to ~10 kpc (P17b), see Section 3.4.

JW100, or IC 5337, was classified as an AGN by Wong et al. (2008), based on X-ray Chandra observations. It was classified as a head-tail radio source by Gitti (2013), who detected radio emission in Very Large Array radio measurements at 1.4 and 4.8 GHz: the peak of the radio emission coincides with the MUSE centre. Double-peaked profiles are detected in the region around the nucleus (P17b).

JO175, **JO206** (P17a), **JO194**: in these galaxies emission lines appear as single-component Gaussians.

We refer to P17a for a detailed description of the GASP survey, data, and adopted reduction techniques. Observations were obtained with the MUSE spectrograph in wide-field mode with natural seeing (Bacon et al. 2010). One or two MUSE pointings per galaxy, each with a 2700 s exposure and covering a 1×1 arcmin^2 field of view, are sampled with 0.2×0.2 arcsec^2 pixels over the spectral range 4800–9300 Å with a spectral resolution FHWM ~ 2.6 Å. Data were taken under clear dark sky conditions, with <1 arcsec seeing (Table 1). We remind the reader that the fitting of emission lines in GASP was done using KUBEVIZ (Fossati et al. 2016). Velocity and velocity dispersion were derived from the fit of the lineset consisting of Hα and the [N II] λλ6548 6583 doublet, and used for all other lines; as necessary, one or two Gaussian components were adopted. Emission line velocity dispersions ($\sigma_{\rm obs}$) were corrected for the instrumental component: $\sigma = \sqrt{\sigma_{\rm obs}^2 - \sigma_{\rm inst}^2}$; $\sigma_{\rm inst}$ was derived at each wavelength using a third-order polynomial fit of the MUSE resolution curve (Fumagalli et al. 2014). In the following, we will use the data cube average filtered with a 5×5 pixel kernel in the spatial direction, unless otherwise stated, having subtracted the stellar underlying spectrum fitted with the SINOPSIS code (Fritz et al. 2017). The stellar kinematics is derived with the PPXF code (Cappellari & Emsellem 2004) using stellar population templates from Vazdekis et al. (2010), see P17a for details. The galaxy centre was defined as the centroid of the continuum map obtained by the KUBEVIZ best-fitting model in the Hα region.

All the line fluxes, selected to have a signal-to-noise ratio SN > 3, were corrected for dust extinction using the Balmer decrement as in P17a. Fig. 3 displays the extinction map (A_v) in each galaxy, as well as the electron density ($n_{\rm e}$): this was derived using the relations in Proxauf, Öttl & Kimeswenger (2014), as in P17a. We detect increased values of the extinction ($A_v > 2$) in the central spaxels of JO135, JO204, JO206, and JW100. In JO201 the extinction is low in the nucleus ($A_v < 1$). In JO194 the extinction is high ($A_v > 2.5$) in an extended region of radius ~3 arcsec around the central spaxel. JO201, JO204, and JO135 show a steep increase in density ($n_{\rm e} > 10^{2.5}$ cm^{-3}) in the nucleus: lower densities are measured in JO206 and JW100 ($n_{\rm e} \sim 10^2$ cm^{-3}), and JO194, JO175 ($n_{\rm e} < 10^2$ cm^{-3}).

3 IONIZATION MECHANISMS

The left-hand panels of Fig. 4 present the classification in H II-regions, Composite, AGN, and Liners based on [N II] λ6583/Hα versus [O III] λ5007/Hβ as in P17b, whose main conclusions are summarized here. In some cases (JW100, JO135,[1] JO201, JO204) one Gaussian was not enough to fit the emission line profiles and a double-Gaussian fit was adopted: in these cases, the classification displayed in Fig. 4 refers to the narrow component.

---

[1]Compared to P17b, we improved the fitting of the lines of the central spaxels of JO135.

Table 1. The table shows: the galaxy ID, the host cluster name, redshift and scale, the coordinates of the central spaxel, the seeing, the classification (AGN/LINER/SF) assigned in P17b and, for galaxies classified as AGN or LINER, the estimated AGN sizes and the observed and dereddened [O III] λ5007 luminosities within r_{NLR}.

Id	Cluster	z_{cl}	Scale	RA	Dec.	Class	Seeing	r_{NLR}	r_{AGN}	$\log L_{[\mathrm{O\,III}]}$	$\log L_{[\mathrm{O\,III}]}^{\mathrm{corr}}$
			(kpc arcsec^{-1})				(arcsec)	(kpc)	(kpc)	(erg s^{-1})	(erg s^{-1})
JO135	A3530	0.05480	1.07	12 57 04.2	− 30 22 30.0	AGN	0.73	0.8	3.7	41.24 ± 0.03	42.16 ± 0.03
JO175	A3716	0.04599	0.90	20 51 17.6	− 52 49 21.8	SF	1.05				
JO194	A4059	0.04877	0.95	23 57 00.7	− 34 40 50.4	LINER	0.82	0.6	0.7	38.25 ± 0.01	39.30 ± 0.01
JO201	A85	0.05568	1.08	00 41 30.3	− 09 15 45.9	AGN	0.99	1.1	3.7	41.90 ± 0.02	42.20 ± 0.02
JO204	A957	0.04496	0.88	10 13 46.8	− 00 54 50.9	AGN	0.87	0.7	1.8	40.29 ± 0.02	41.25 ± 0.02
JO206	IIZW108	0.04889	0.96	21 13 47.4	+02 28 34.1	AGN	1.14	1.0	2.6	40.78 ± 0.02	41.41 ± 0.02
JW100	A2626	0.05509	1.07	23 36 25.0	+21 09 02.5	AGN	1.09	1.3	2.8	40.37 ± 0.02	40.79 ± 0.02

Based on the P17b analysis, JO201, JO204, JO206, JO135, and JW100 present AGN-like line ratios in the inner kpc. None of them show broad (>5000 km s^{-1}), permitted lines typical of the broad-line region in AGN; the observed emission lines are therefore produced in the narrow-line region (NLR). Extended AGN-like emission over several kpc is observed in JO204 and JO135, and it can be attributed to anisotropic ionization from the AGN (the so-called ionization cones). In JO175 the emission is mostly due to star formation, while in JO194, composite line ratios are detected throughout the galaxy.

We define the size of the NLR in the AGN candidates as in Bae et al. (2017), that is weighting the projected distances from central spaxel on the [O III] λ5007 fluxes, over the spaxels classified as AGN in P17b:

$$r_{\mathrm{NLR}} = \sum_{r<5\mathrm{Kpc}} r f_{[\mathrm{O\,III}]}(r) / \sum_{r<5\mathrm{Kpc}} f_{[\mathrm{O\,III}]}(r), \qquad (1)$$

r being the distance from the central spaxel and $f_{[\mathrm{O\,III}]}$ the line flux at that distance. The NLR size so defined is of the order of 1 kpc for all galaxies: as the typical seeing was ∼0.8–1 arcsec, the NLR is unresolved. To have an estimate of the maximum extension of the AGN-ionized region, we also computed the 95 per cent percentile of the distances for the AGN spaxels (r_{AGN} in Table 1), keeping in mind that these values may be biased by spaxels with fainter [O III] fluxes, where the measurement uncertainties may produce a wrong classification. The AGN emission can be therefore described as the sum of a pointlike source producing the bulk of the emission and a fainter, extended ($r > 1$ kpc) emission.

3.1 Photoionization and shock models

We now complement the classification done in P17b with a more de-tailed analysis: we simultaneously consider the lines (H α, H β, [O I] λ6300, [O III] λ5007, [N II] λ6583, [S II] λλ6717,6731) commonly used to identify AGN (Veilleux & Osterbrock 1987; Kewley et al. 2006) and compare them to the predictions from photoionization and shock models. In those cases where two components were required for the fit, we considered the summed fluxes for the comparison with models.

We proceed as follows: (1) we selected only spaxels classified in P17b as either AGN, composite, or LINERs; (2) for each spaxel we run NEBULABAYES (Thomas et al. 2018), a PYTHON code that adopts a Bayesian approach to select the model optimally fitting the target emission line fluxes.

NEBULABAYES includes grids where constant gas pressure pho-toionization models are computed with the MAPPINGS V code, for

H II regions and AGN. A full discussion of the assumptions and parameters of these models is given in Thomas et al. (2018), we summarize here the main aspects.

For H II regions, the ionizing continuum is defined by the SLUG2 (Krumholz et al. 2015) stellar population synthesis code, with five metallicities ($Z = 0.0004, 0.004, 0.008, 0.02, 0.05$). For AGN, the ionizing continuum is described in Thomas et al. (2016), and is parametrized by the energy of the peak of the accretion disc emission (E_{peak}), the photon index of the inverse Compton scattered power-law tail (Γ), and the proportion of the total flux in the non-thermal tail (p_{NT}). In the grid models, the latter two parameters are fixed (Γ = 2, $p_{\mathrm{NT}} = 0.15$).

For both H II regions and AGN, the other model free parameters are: the metallicity ($12 + \log$ O/H), the ionization parameter (U), and the gas pressure ($\log P/k$), with $P/k \sim 2.4 n_{\mathrm{e}} T$, see e.g. Kakkad et al. (2018).

Considering the environment of these galaxies and the presence of outflows in the nuclear regions, it is important to understand what may be the contribution from shocks, and if shocks alone can produce the observed line ratios. As extensively discussed by Allen et al. (2008), in the so-called fast shock models the cooling of the hot gas behind the shock front produces high-energy photons which ionize the pre-shocked gas (precursor). When the shock velocity is >170 km s^{-1}, the contribution from the photoionized gas in the precursor starts to become increasingly important and both high and low ionization lines are present in the observed spectrum. Varying the input model parameters, that is the pre-shock density, n, the shock velocity, v_{s}, the pre-shock transverse magnetic field, B, and the gas atomic abundances, it is possible to produce a wide range of emission line ratios, from H II-like regions to Liners and AGN.

Since shock model libraries are not directly available in NEBULA-BAYES, we adapted the Allen et al. (2008) fast shock grids so that they could be used in NEBULABAYES. From these grids, we selected the models with[2] $n = 0.1, 1, 10$ cm^{-3}, for which solar ($n = 0.1, 1, 10$ cm^{-3}) and 2× solar ($n = 1$ cm^{-3}) abundances are available.

For each model type (shock, H II and AGN), NEBULABAYES was run spaxel by spaxel, providing as output the best-fitting model line ratios and the χ^2: the optimal model was selected as the one giving the lowest χ^2. We stress that different reasons may contribute to produce the wrong classification for a given spaxel, as for instance the uncertainties on the line measurements, the limited number

---

[2] We remind that the pre-shock density is not directly related to the electron density measured e.g. by the [S II] λλ6716, 6731 lines, giving the post-shock density (see e.g. Dopita & Sutherland 1995).
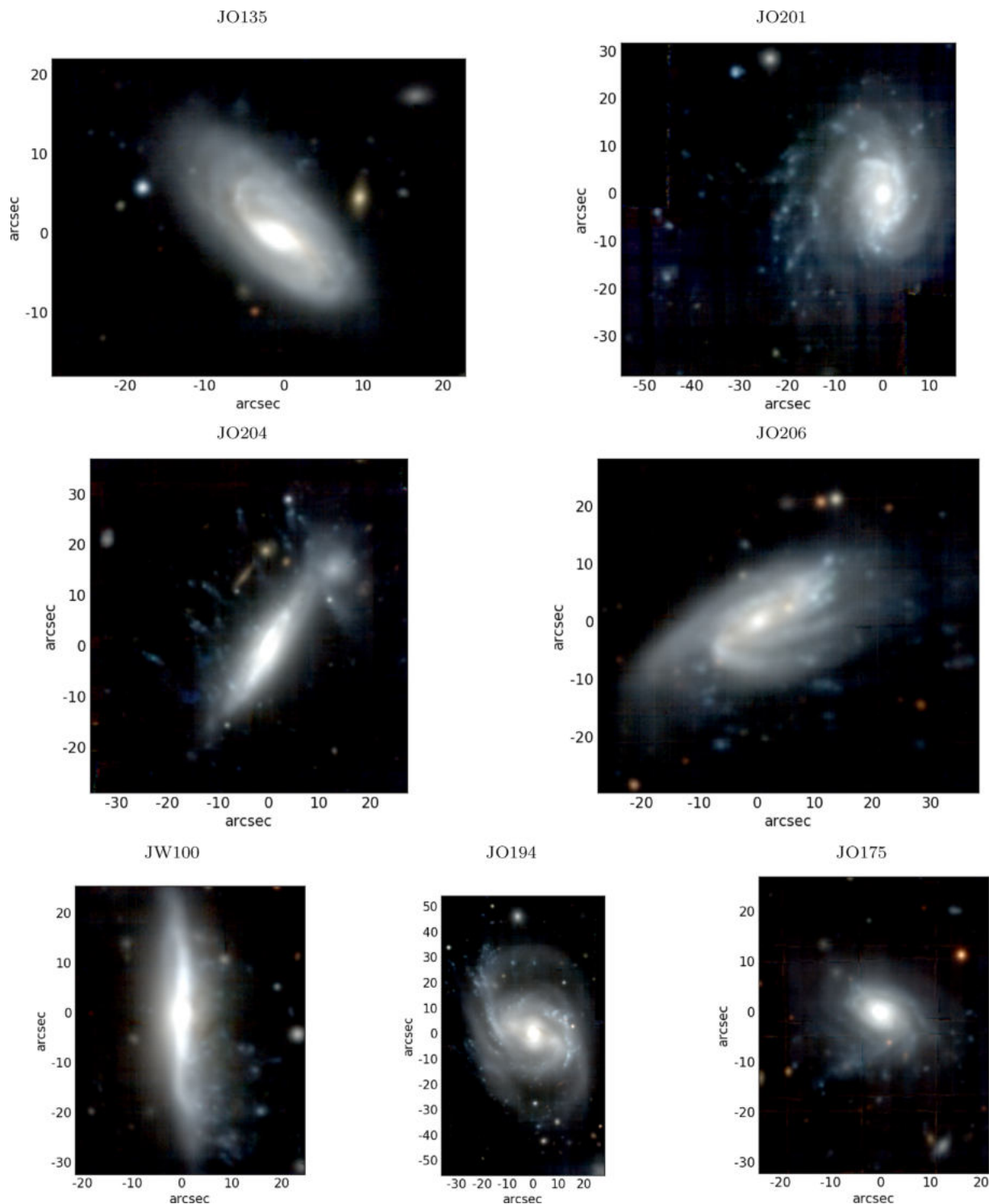
Figure 1. VRI images built from the MUSE cubes for the seven galaxies analysed in the paper.

of parameters in the models, and the fact that in many cases we may have at the same time a contribution from different ionizing mechanisms.

3.2 Results: shock versus AGN

Fig. 5 presents AGN and shock model grids overlaid on the observed spaxel line ratios; the latter are colour coded with the distance

from the galaxy centre. For AGN models, we display those with $\log E_{\mathrm{peak}} = [-0, 5, 0, +0.5]$ around the best-fitting value of the central spaxel, and for different values of $\log U$. The abundances in the nucleus derived from the NEBULABAYES fits are supersolar $(12 + \log \mathrm{O/H} > 9)$ in the AGN-dominated nuclei, and are Solar $(12 + \log \mathrm{O/H} = 8.76)$ outside. For fast shock models, we plot a grid of varying velocities and magnetic field values, fixing the best-fitting density and metallicity.
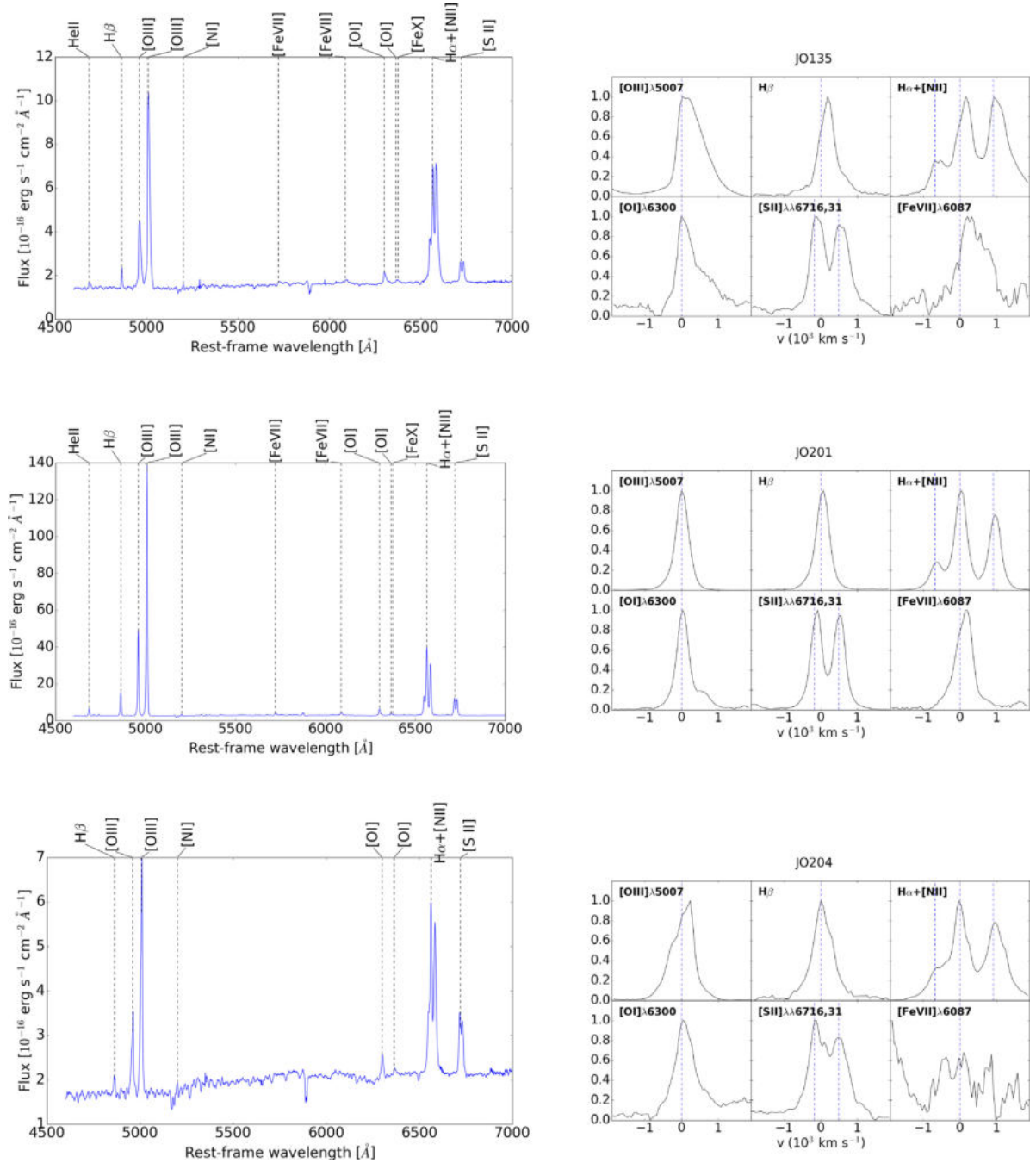
Figure 2. The plots show for the central spaxel of each galaxy: *left* – the uncorrected spectra with the identification of the main emission lines; *right* – the normalized line profiles after the subtraction of the stellar underlying spectrum as described in the text: the dashed lines indicate the assumed galaxy velocity. A meaningful detection (SN > 3) of [Fe VII] λ6087 is seen only in JO135 and JO201.

The maps of the best-fitting classification from NEBULABAYES, compared with the classification derived as in P17b, are displayed in Fig. 4.

Fast shock models in individual diagnostic diagrams can produce a wide range of line ratios, covering both the H II and AGN regions of the diagrams. For the most extreme cases like JO135 and JO201 that have log [O III]/Hβ ∼ 1, in order to reach the observed line ratios the shock models require $v_{sh} > 500 \, \mathrm{km \, s^{-1}}$ while in our case the width of the strongest component is $\sigma_v \sim 100 \, \mathrm{km \, s^{-1}}$. When log [O III] λ5007/Hβ is low (<0.5)

the shock velocities do not need to be so extreme. However, as shown in Fig. 5, for JO135, JO201, JO204, JO206, JW100, shock models produce either too high [O I] λ6300/Hα ratios or too low [N II] λ6583/Hα ratios, while AGN photoionization models reproduce all diagnostic ratios, as found for typical AGN by Allen et al. (2008).

For JO194 the emission line ratios fall in the LINER side of the diagrams, with log [O III] λ5007/Hβ ≤ 0.2, where optical lines alone are not able to clearly separate between AGN and other ionization mechanisms (see e.g. Belfiore et al. 2016). Around the central spaxel
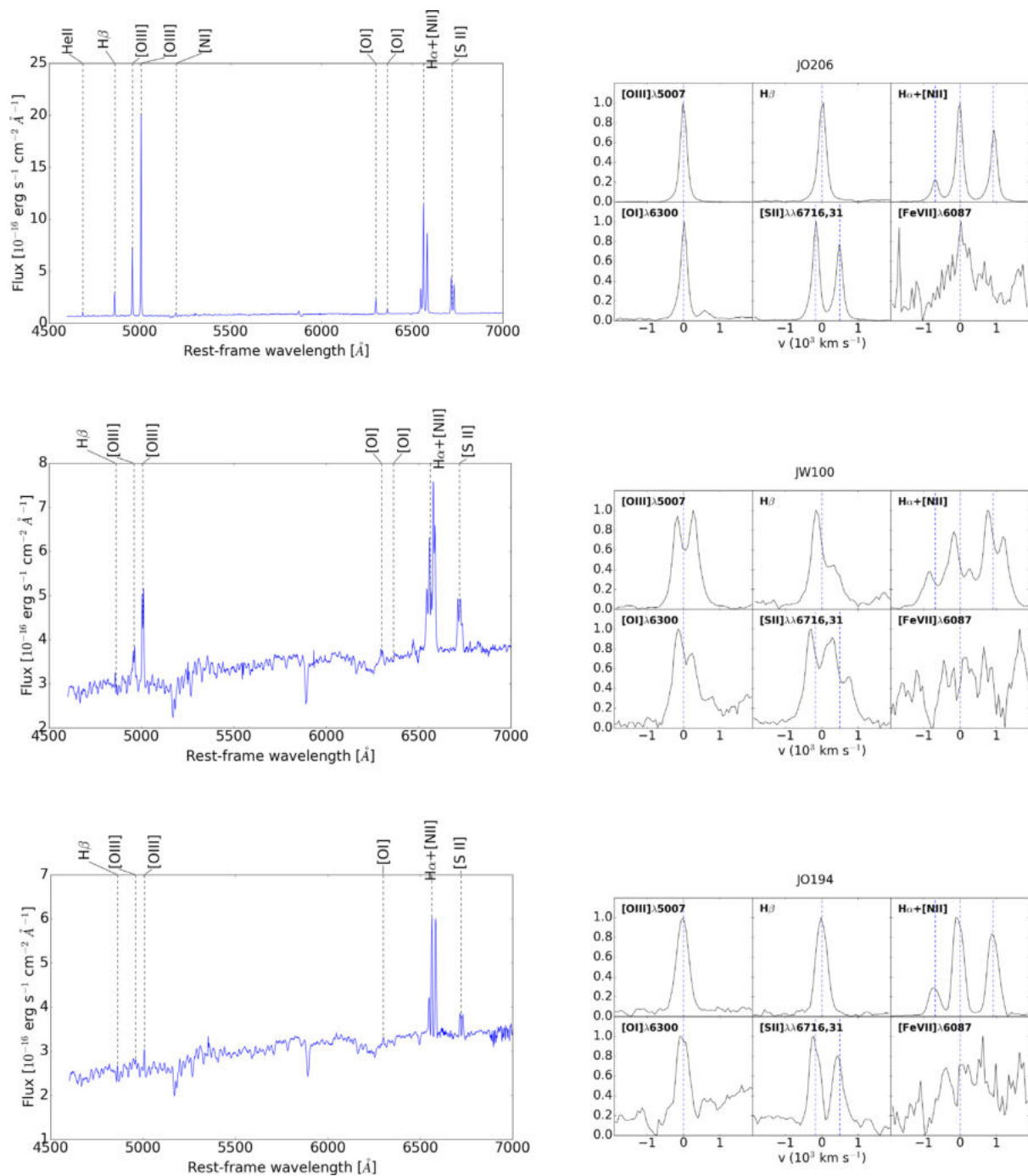
Figure 2 – *continued*

there is a very small region, whose size is few spaxels, where AGN models produce a lower χ^2 than shock models. However, as displayed in Fig. 4 the line ratios move to the SF region of the diagrams already within 2 kpc; line ratios similar to what observed in the nucleus are also present up to ∼5 kpc. Considering the uncertainties due to the fact that here we do not consider mixed models where both SF and AGN or shocks contribute to the line ratios, we conclude that we cannot confirm or discard the presence of the AGN; in P17b the AGN option was favoured, considering the high Chandra X-ray luminosity ($L_{0.3-8keV} = 1.4 \times 10^{41}$ erg s^{-1}). Since we detect a strong extinction ($A_v > 2.5$) in the nuclear regions, it is possible that AGN emission is obscured by dust in the optical.

For JO175, line ratios are consistent with star formation, as well as with some of the shock models as suggested by the high [O I] $\lambda6300$/Hα ratio, but not with an AGN.

As a further test, we compare the observed, dust corrected L(Hβ) luminosity within r_{NLR} with the value derived from the Allen et al. (2008) library, selecting models with $n = 1$ cm^{-3} and best-fitting values in the central spaxel for B and v_{sh}. We estimate the maximum contribution from shocks to be negligible (<3 per cent) for JO135, < 20 per cent for JO194, JO201, JO204, and JO206, < 40 per cent for JW100.

We conclude that, in agreement with P17b, the NEBULABAYES results confirm that the central spaxels of all galaxies except JO175
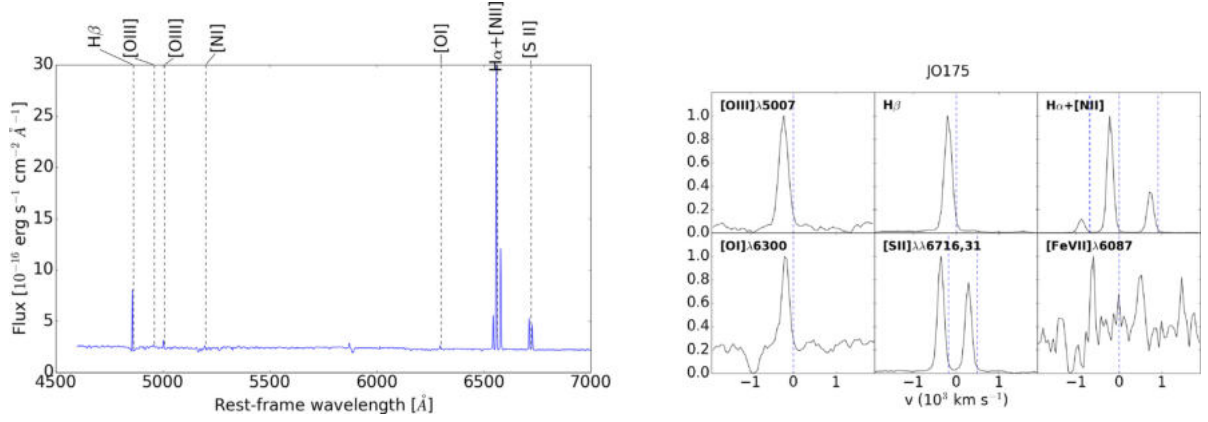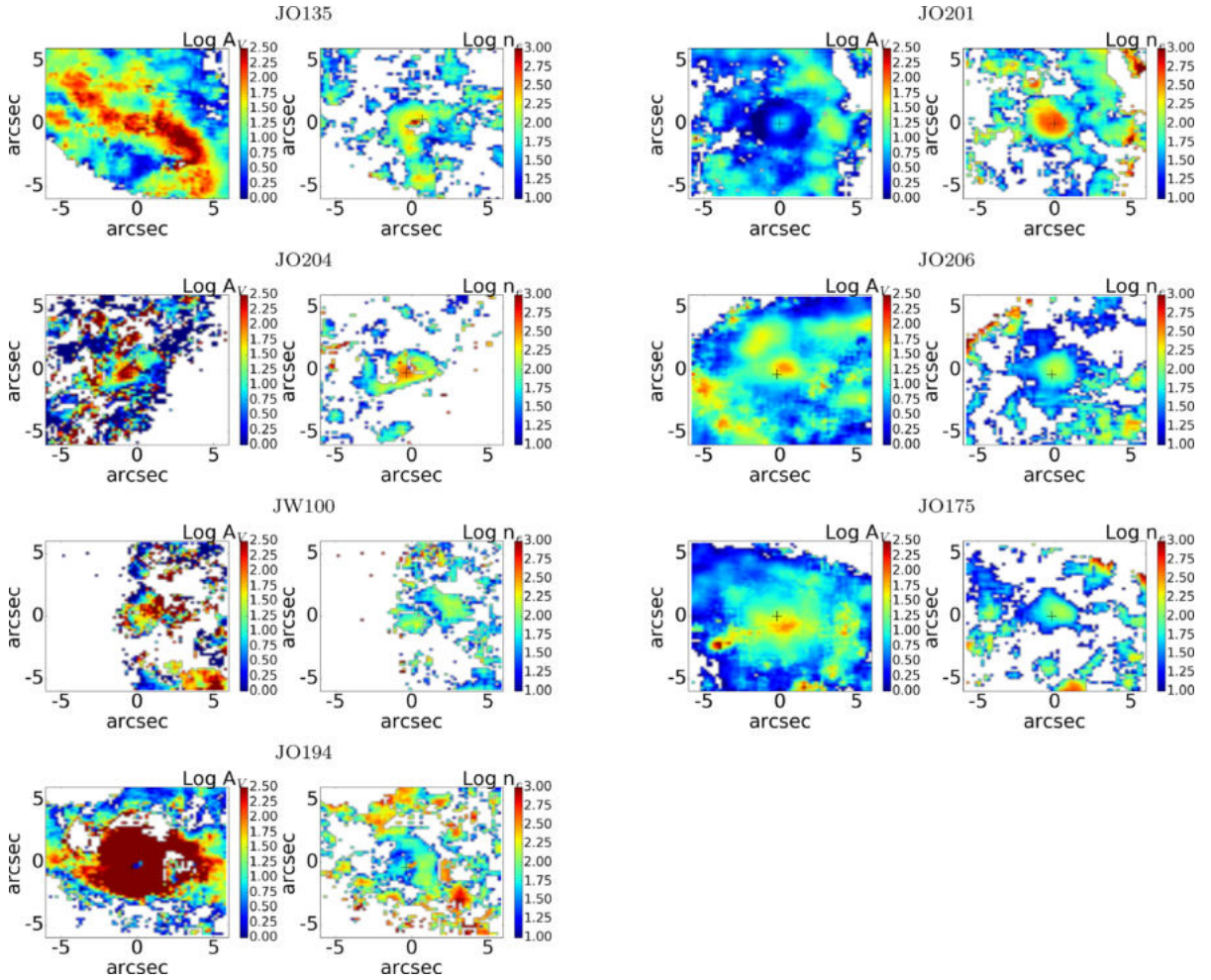
Figure 2 – *continued*

Figure 3. For each galaxy the plots show the spatial distribution in the central 10×10 arcsec^2 of *left:* extinction (A_v), *right:* $\log n_e$. For all galaxies, 1 arcsec is ∼1 kpc (see Table 1).

are best fitted by AGN models, whose parameters are given in Table 2. For JO175, nuclear line ratios can be fitted either by SF or by shocks: H II-like [N II] $\lambda6583$/Hα and [S II] $\lambda\lambda6716 + 6731$/H$\alpha$, but high [O I] $\lambda6300$/Hα, agree well with shock models (either fast or slow).

Finally, four galaxies (JO201, JO204, JO206, and JW100) also show AGN line ratios in the circumnuclear regions (<5 kpc),

with an expected decrease of the ionization parameter, and a decrease of E_{peak} consistent with an increasing contribution from H II (*composite*) regions. In fact, as discussed in Thomas et al. (2018), variations in E_{peak} may be due either to screening by gas and dust (hardening the ionizing continuum and thus increasing E_{peak}), or to contamination from shock or H II regions (softening the continuum and thus decreasing E_{peak}).
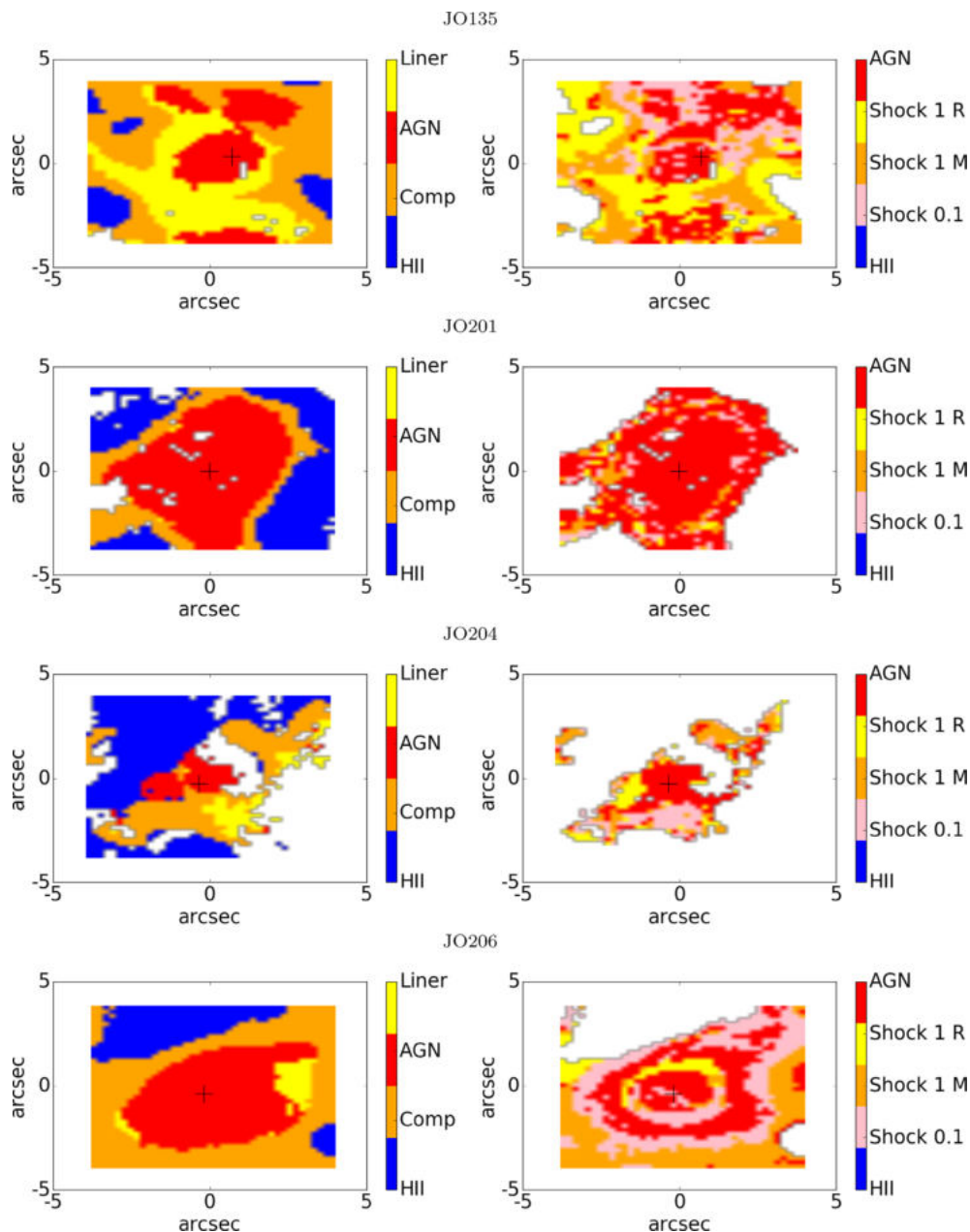
Figure 4. Colour coded maps in a region of 100×100 spaxels around the nucleus. *Left*: classification from P17b (H II, composite, AGN, LINER). *Right:* NEBULABAYES models: H II; shock with $n = 0.1$ cm^{-3}, solar abundances; shock with $n = 1$ cm^{-3}, solar abundances (M); shock with $n = 1$ cm^{-3}, $2\times$ solar abundances (R); AGN. Spaxels classified as H II in P17b were not fitted with NEBULABAYES.

3.3 Coronal lines

The high ionization (coronal) line [Fe VII] $\lambda 6087$ (Figs 2 and 6) is detected in the inner kpc region of JO201 and JO135, with a peak SN of ~ 20, corresponding to [Fe VII] $\lambda 6087$/H$\alpha \sim 0.05$. The weaker lines [Fe VIII] $\lambda 5721$ and [FeX] $\lambda 6375$ (blended with [O I] $\lambda 6363$) are also present in the same regions. We report the presence in JO206 of a faint feature in the [Fe VII] $\lambda 6087$ spectral region, but the SN < 3 is too low for a sure identification. Both in JO135 and JO201, the [Fe VII] $\lambda 6087$ line is characterized by a profile similar to that of low ionization lines, but it has a redshifted peak with respect to the Balmer recombination lines, in particular in JO201, suggesting that these lines are produced in different regions. This is confirmed by the fact that, compared to

the other lines, its emission is concentrated (Fig. 6) in a region whose size is close to the size of the PSF (FWHM ~ 1 arcsec). Adopting the definition of the NLR size presented before, we obtain r_{NLR}(Fe VII) < 0.5 kpc, and r_{AGN}(Fe VII) ~ 0.5 kpc (JO135), 1.2 kpc (JO201): it is therefore unresolved in JO135, while in JO201 there is a faint extended emission that could be however an artefact due to the PSF wings. The intensities of coronal lines are not available in the NEBULABAYES grids, since MAPPINGS does not accurately model these lines (Davies et al. 2016). Different models were presented to reproduce coronal lines in AGN. Mingozzi et al. (2019) reported the presence of Fe coronal lines in a sample of AGN with outflows, observed with MUSE: they attributed them to the inner, optically thin and highly ionized regions of
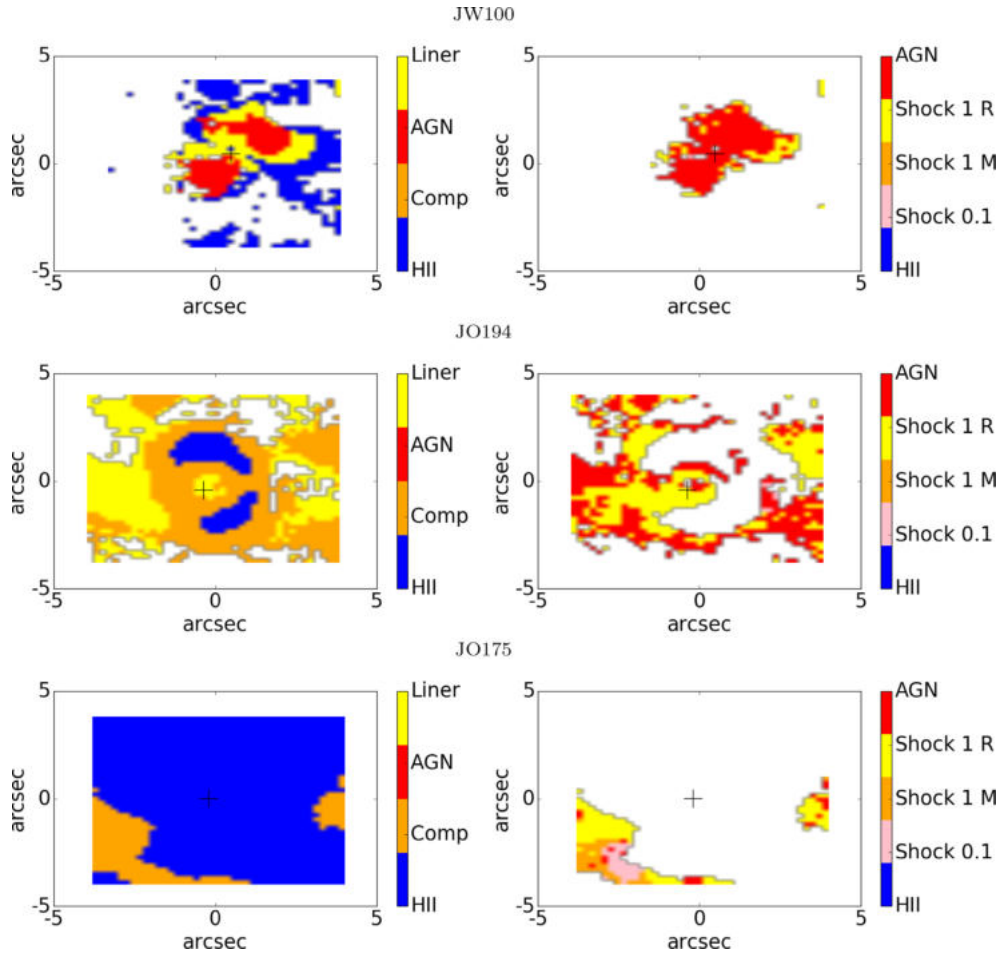
Figure 4 – *continued*

the outflows. Korista & Ferland (1989) attributed them to a low-density ($n_e \sim 1$ cm^{-3}) ISM heated by the AGN radiation, in a region whose size is similar or larger than the NLR ($\sim$1–2 kpc). Ferguson et al. (1997) and Komossa & Schulz (1997) showed that multicomponent photoionization models, where emission lines are produced in an ensemble of clouds with different gas densities and distances from the centre, are able to successfully fit the observed values: in particular, in these models coronal lines are mostly produced by hot ($T \sim 10^5$ K) gas heated by the AGN in the high-ionization inner regions (see also Mazzalay, Rodríguez-Ardila & Komossa 2010). Thomas et al. (2017) reported the existence of a correlation between [Fe VII] $\lambda6087$/Hα and [O III] $\lambda5007$/Hβ in Seyfert galaxies in their sample, that they interpreted as an effect of a radiation pressure dominated environment, where Compton heating in the central regions triggers the production of coronal lines (Davies et al. 2016). Consistently, both JO201 and JO135 show a high [O III] $\lambda5007$/Hβ (>10) ratio in the inner regions where the emission of [Fe VII] is observed. The absence of this line in the other galaxies may be due either to orientation effects preventing us to see the inner regions, or to an intrinsic difference in the properties of the ionized gas.

3.4 Extranuclear regions

AGN-like regions are detected in JO135 and JO204 (Gullieuszik et al. 2017) up to $\sim$20 kpc from the nucleus (Fig. 7), with high

values of [O III]/H$\beta \sim 10$ (Fig. 5). This is typical of the so-called Extended Emission Line Regions (EELR; see e.g. Yoshida et al. 2004; Maddox 2018), where the gas ionized by the AGN extends over scales of tens of kiloparsecs.

In these regions the [S II] $\lambda6716/\lambda6713$ ratio, close to $\sim$1.4, indicates low values of the electron density ($n_e < 50$ cm^{-3}), and the emission line widths are close to the instrumental value. The line ratios could be reproduced by shock models with $n \sim 0.1$ cm^{-3}, but the required shock velocity, $V_{sh} > 400$ km s^{-1}, is too high compared to the observed values: this rules out the presence of fast shocks (see also Fu & Stockton 2009), and favours photoionization from the AGN (Fig. 5).

In JO204, the required ionization parameter in the outer regions ($\sim$15 kpc) is close to the value derived in the nuclear ($r < 2$ kpc) regions (log $U \sim -3$). A nearly constant ionization parameter implies that the photon flux and the gas density should both decrease as r^{-2}. This is consistent if there is a coupling between the radiation and the illuminated gas, as in the case of radiation pressure mechanisms (Thomas et al. 2018). The best-fitting AGN models indicate for JO204 log $P/k \sim 7$ in the nucleus ($r \sim 1$ kpc), log $P/k \sim 4.6$ at 15 kpc: this would be consistent with $n_H \sim r^{-2}$, suggesting that the low-density gas in the ISM may be ionized by anisotropic radiation from the AGN. In order to verify if we can reproduce the observed Hβ luminosities, we proceed as follows. For a gaseous cloud, the rate (photons s^{-1}) of ionizing photons required to produce the observed, dereddened Hβ luminosity (erg
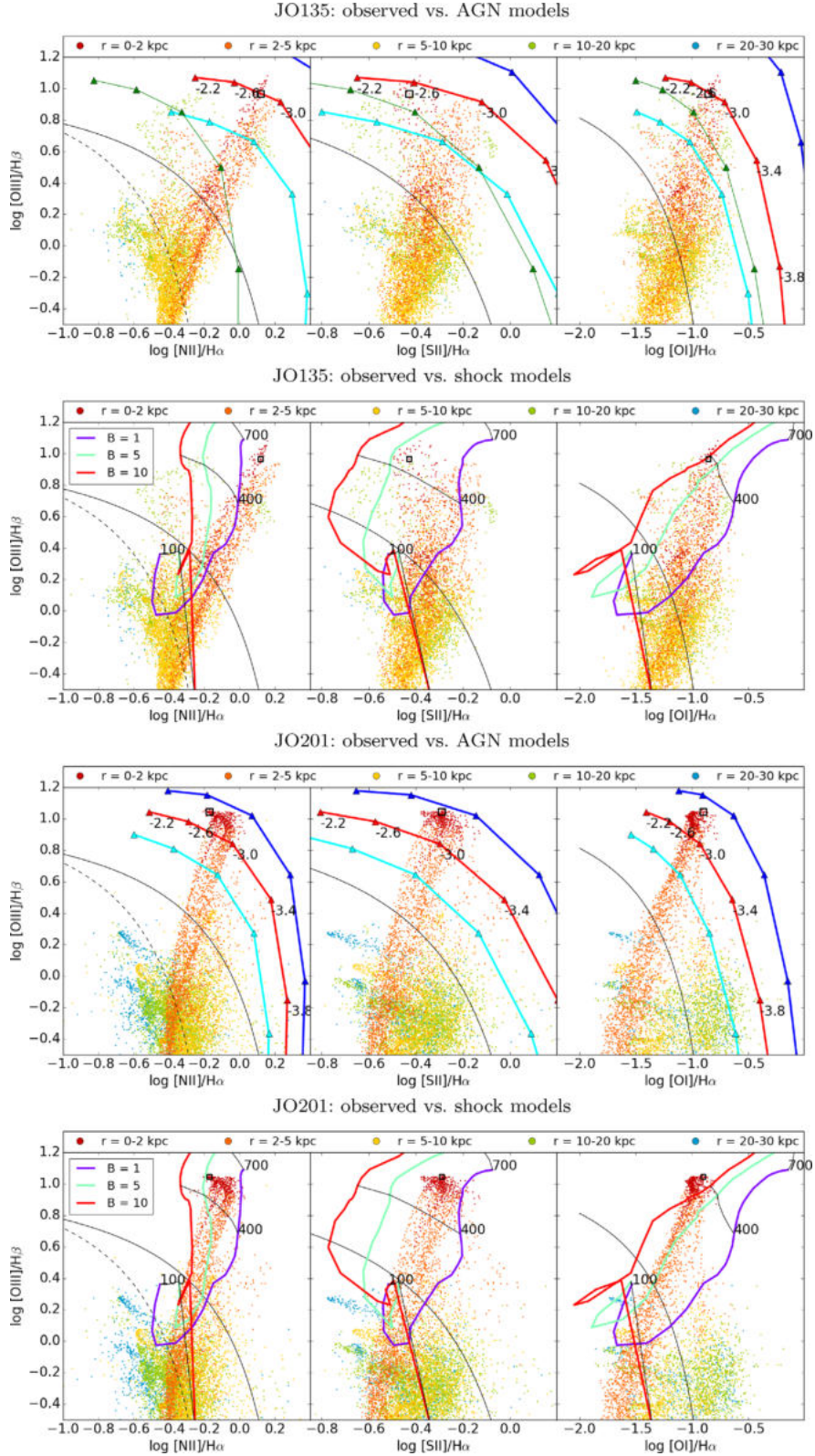
Figure 5. Observed emission line ratios colour coded with the projected distance from the centre; the empty square displays the value measured in the central spaxel. The black solid and dashed ([N II]/H α panel) curves indicate the empirical SF/Composite/AGN classification by Kewley et al. (2006). For each galaxy, overlaid are best-fitting AGN (not for JO175) and shock models. **AGN models** – The red lines display models for different values of log U, adopting the best-fitting values of log P/k, $12 + \log$ O/H and $E_{\rm peak}$ in the central spaxels; models with an offset ± 0.25 in $E_{\rm peak}$ are displayed in cyan and blue, respectively. For JO204 and JO135, the green line shows AGN models in the EENLR. **Shock models** – The lines display models for $v_{\rm sh} = 100$–700 km s^{-1}, pre-shock density $n = 0.1$ cm^{-3}, solar abundances (JO135, JO201, JO206); $n = 1$ cm^{-3}, $2\times$ solar abundances (JO204, JW100, JO175, JO194), and magnetic field B as in the legend.
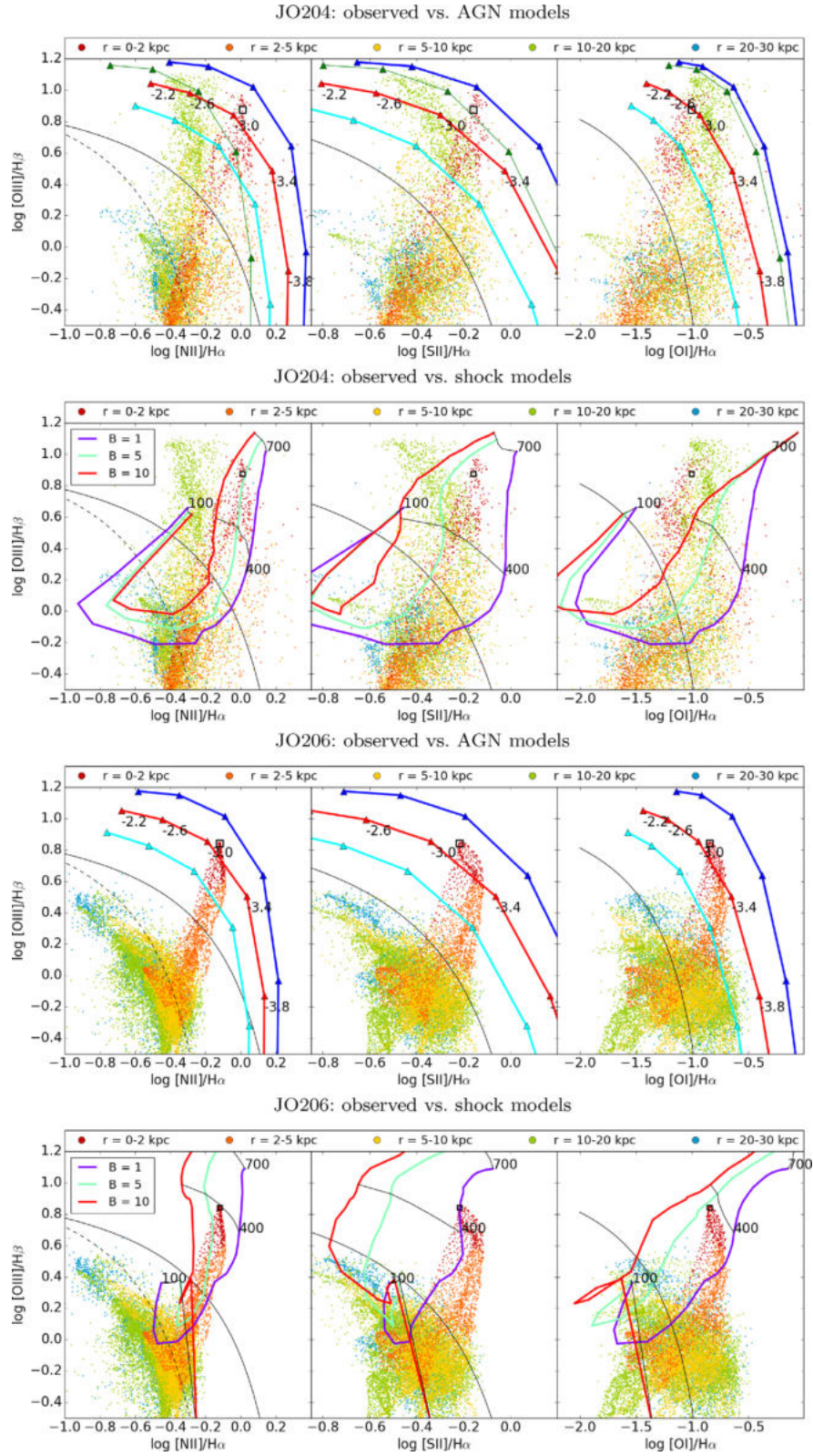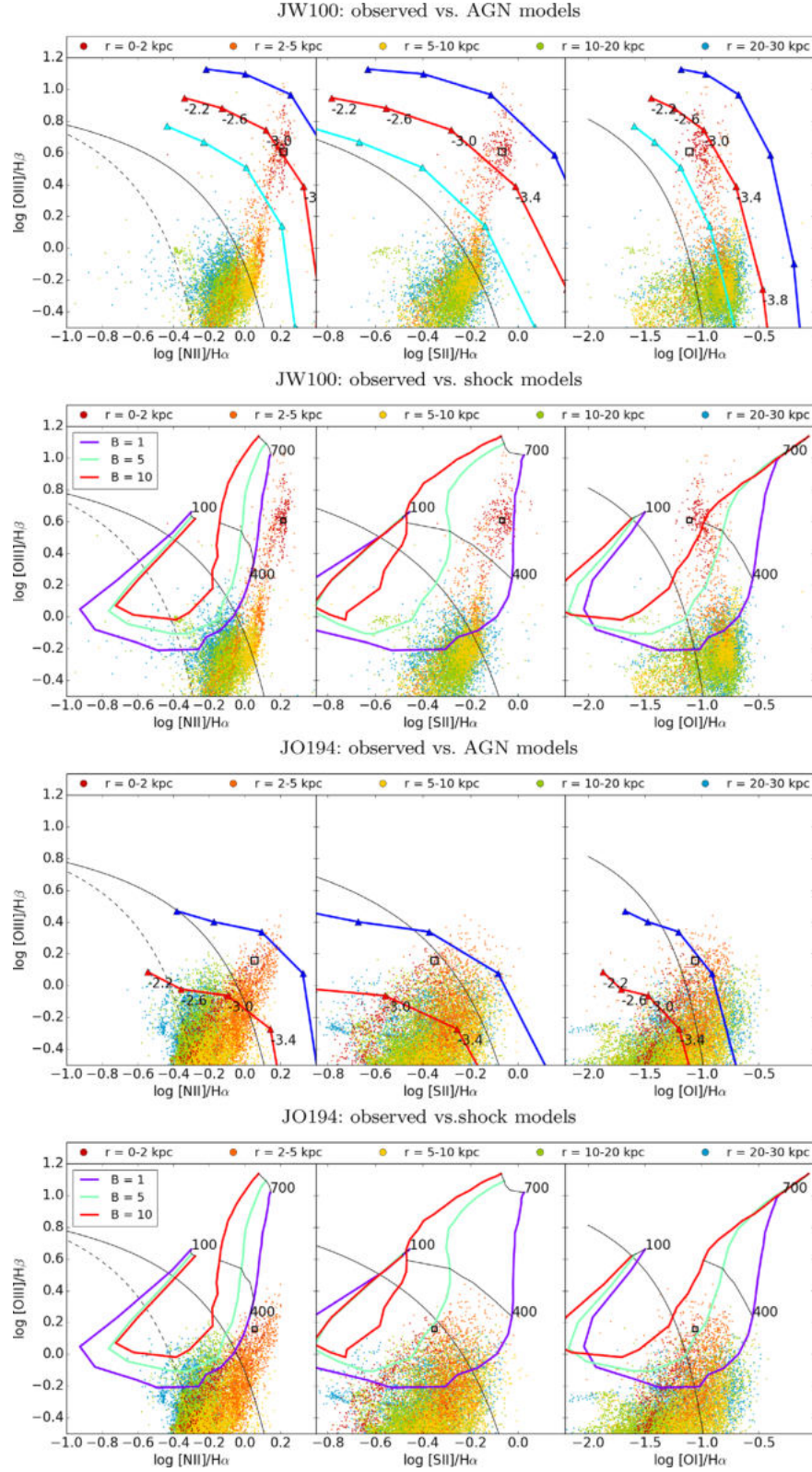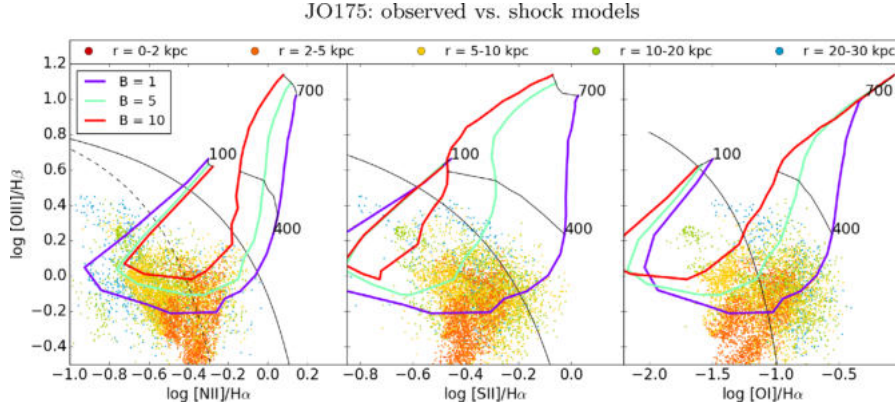
Figure 5 – *Continued*

Figure 5 – *Continued*

Figure 5 – *Continued*

Table 2. Best-fitting parameters for the nuclear AGN photoionization models.

Id	$\log P/k$	$\log E_{peak}$	$12 + \log O/H$	$\log U$
JO135	6.6	−1.2	9.16	−2.49
JO201	7.0	−1.5	8.99	−2.77
JO204	7.0	−1.5	8.99	−3.06
JO206	6.6	−1.5	8.87	−3.06
JW100	7.0	−1.5	9.15	−3.06
JO194	6.2	−1.7	9.30	−3.34

s^{-1}) is (Osterbrock & Ferland 2006):

$$Q(H^0) = \frac{L(H\beta)}{h\nu_{H\beta}} \frac{\alpha_B(H^0, T)}{\alpha_{H\beta}^{eff}(H^0, T)} \sim 2.09 \times 10^{12} L(H\beta) \quad (2)$$

where $L(H\beta)$ is the observed, dereddened H β luminosity (erg s^{-1}); in the Case B approximation $\alpha_B(H^0, T) = 2.59 \times 10^{13}$ cm^3 s^{-1}, $\alpha_{H\beta}^{eff}(H^0, T) = 3.03 \times 10^{14}$ cm^3 s^{-1} ($T \sim 10^4$ K).

We can thus derive the rate of ionizing photons that should be emitted by the nucleus:

$$Q(H^0)_{nuc} = Q(H^0) \left(\frac{\Omega}{4\pi}\right)^{-1} \quad (3)$$

where Ω is the solid angle covered by the extranuclear region, that is $\Omega = A/d^2$, for a region of area A and projected distance d from the nucleus. From the H β fluxes measured in the EENLR of JO204 at 15 kpc, we obtain[3] $Q(H^0)_{nuc} \sim 10^{54}$ ph s^{-1}: using this value to compute the ionization parameter, we obtain $\log U \sim -3$ for $n_H \sim 1$ cm^{-3}, in agreement with the value expected from photoionization models. Similar results are obtained for JO135.

4 GAS PROPERTIES: DISC AND OUTFLOW COMPONENTS

As discussed before, in four galaxies (JO201, JO204, JW100, and JO135) emission lines in the circumnuclear regions are characterized by complex profiles that require at least two Gaussian components to be fitted. In order to disentangle the contribution to the emission lines from gas in disc and other components (e.g. outflows), we focus on the [O III] λ5007 line. Compared to the

---

[3]We neglect the factor due to the unknown projection, but here we are interested in order of magnitudes.

H α + [N II] lineset used in P17b, [O III] is more suitable for this analysis as it is not affected by the presence of other nearby emission lines (the [N II] doublet in the case of H α) or by possible residual broad components in the inner AGN regions, as it may be the case for permitted lines, and better traces the ionized gas in the outflows (see e.g. Bae & Woo 2014, and refs). To this end, we selected a region of $\sim 10 \times 10$ arcmin^2 around the centre of each galaxy and fitted the [O III] λ5007 line, using the functions available in the PYTHON library lmfit. For each spaxel, we made the fit adopting both one and two Gaussian components. The two-component solution was chosen if it gave an appreciable improvement to the fit compared to the one-component solution: based on visual inspection, we defined this condition as $\chi_{n=1}^2 > 1.5 \chi_{n=2}^2$, χ^2 being the chi-square of the fit (see Davis et al. 2012, for a similar approach), and in addition we requested that the flux in each component must be at least 10 per cent of the summed flux. We also discarded those fits where S/N([O III]) < 5, where the signal S is the total line flux and the noise N is the standard deviation of the fitting residuals.

From the velocities measured at 10 per cent, 50 per cent, and 90 per cent of the cumulative flux percentiles, we used the definitions in Liu et al. (2013) to estimate the parameters introduced by Whittle (1985): the peak velocity of the [O III] line (v_{pk}), the median velocity (v_{50}), the width $W_{80} = v_{90} - v_{10}$ and the asymmetry $A_{sym} = \frac{(v_{90}-v_{50})-(v_{50}-v_{10})}{W_{80}}$. In this definition, positive/negative values of A_{sym} indicate red/blue asymmetric lines. We used the fit to model the line profile and compute these parameters. In this way we do not assign any physical meaning to the decomposition, using the fit only to reduce the effect of the noise on the estimate of the profile parameters (Liu et al. 2013; Harrison et al. 2014; Balmaverde et al. 2016).

The spatial distribution of these parameters for the galaxies showing two emission line components (JO135, JO201, JO204, and JW100) is displayed in Fig. 8, where the velocity measured for stars is also displayed as reference.

For a more quantitative analysis, we then analysed (Fig. 9) the velocity and velocity dispersion of the two fitted components, bearing in mind that the fit may be degenerate, in particular when the components are close, or in the outer regions where the line is fainter and noise may introduce spurious features.

In the presence of an outflow we expect to see a clear separation in both velocity and velocity dispersion between a (primary) component, kinematically dominated by the gravitational potential traced by the stellar component, and a secondary (slightly broader) component with a velocity offset showing its non-gravitational origin (Woo et al. 2016; Karouzos, Woo & Bae 2016a). To check if this
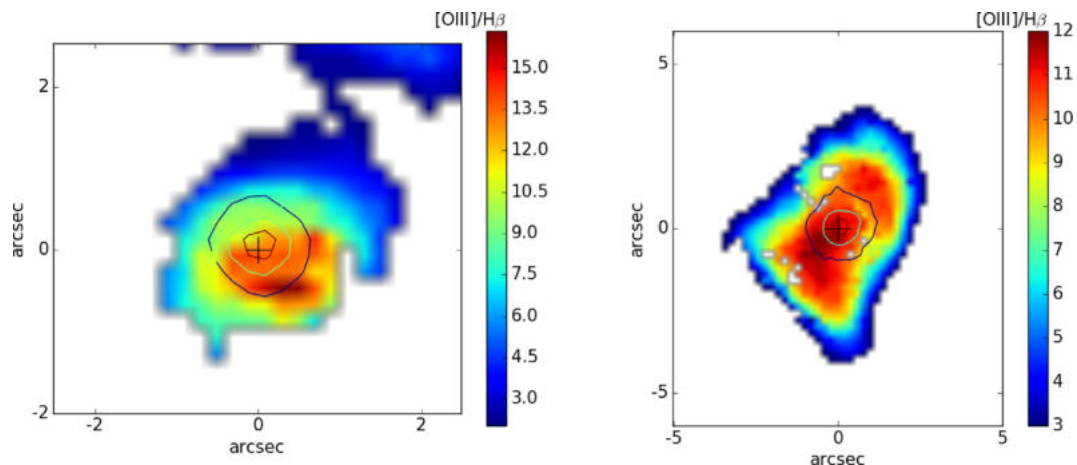
Figure 6. The contour maps showing emission at SN of ∼5–20 in the [Fe VII] λ6087 line are overplotted on the [O III] λ5007/H β map for the nuclear AGN regions of JO135 (*left*) and JO201 (*right*). The cross displays the position of the peak in [O III] λ5007.
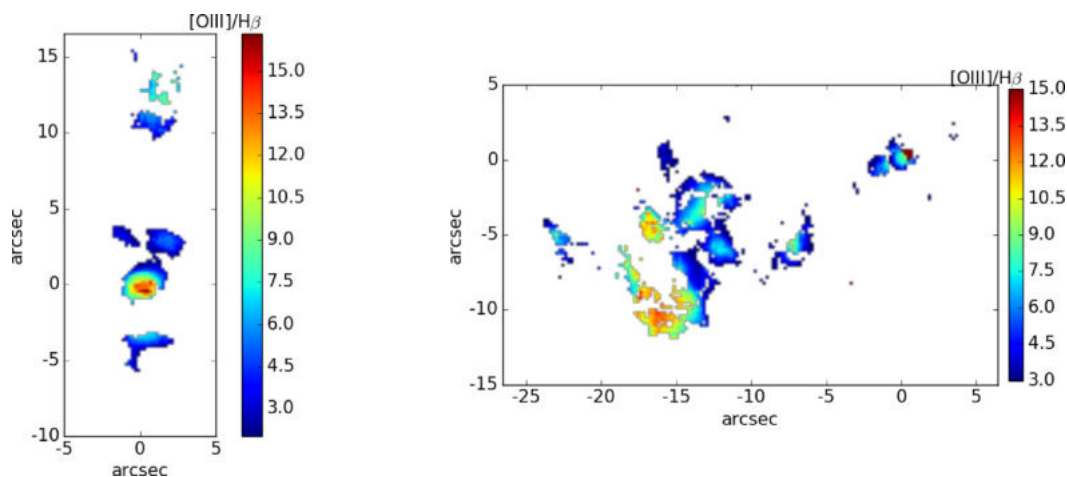
Figure 7. [O III] λ5007/H β maps showing the AGN-like extranuclear emission in JO135 (*left*) and JO204 (*right*). The coordinates are centred on the position of the central spaxel.

is the case, Fig. 10 shows the radially binned values of the deviations from the stellar values of the velocity and velocity dispersion.

As discussed in Crenshaw et al. (2010), the observed line profiles can be explained by a combination of biconical outflows and extinction from dust in the inner galaxy disc. Biconical outflows are most often observed as broad, blueshifted components in the emission lines as the redshifted, receding part of the outflow more likely lies behind the galaxy disc and is thus suppressed by dust. In some cases, instead, red asymmetric lines are observed: this can still happen when the inclination of the disc is such to hide the approaching part of the outflow. In addition, Lena et al. (2015, see their fig. 15) proposed a model where dust is embedded in the outflowing clouds: in this case, blueshifted clouds at small distances from the centre preferentially show their non-ionized face and are thus fainter compared to redshifted clouds, showing instead their ionized face. At large projected distances, an increasing fraction of the ionized face is visible in the blueshifted clouds, which are then brighter.

Figs 8, 9, and 10 demonstrate that the four galaxies with double components have an outflow, and that their outflow properties are quite diverse, as we discuss in the following.

4.1 Outflows properties for individual galaxies

JO135: within a radius ∼1 kpc from the centre, it presents a quite broad [O III] λ5007 ($W_{80} \sim 1000$ km s^{-1}), which is asymmetric in the red (Fig. 8): in the same region, there is an increased dust extinction ($A_v \sim 2$), that also extends in the outer regions (Fig. 3). The presence of dust could point to the model proposed by Lena et al. (2015), to explain the dominant redshifted component in the outflow. Outside this region, the velocity pattern follows the stellar one. This can also be seen in the radial plots of the fitted components (Fig. 10), where at $r > 1$ kpc the velocity and velocity dispersion of the narrow component are very close to the stellar values.

JO201: a broader component ($W_{80} \sim 600$ km s^{-1}) is detected in the inner kpc, with a small blue asymmetry. In the same region, we measure an increase of the dust extinction ($A_v \sim 1$), as well as of the electron density ($n_e \sim 10^3$ cm^{-3}). The velocity and velocity dispersion of the narrow component agree with the stellar values: we therefore identify the narrow component with gas in the disc and the broad blueshifted component with the outflow. The low asymmetry in [O III] may imply a spherical or wide-angle outflow (Liu et al. 2013), allowing to see the inner outflow regions and hence the [Fe VII] λ6087 line, as discussed in Section 3.3.
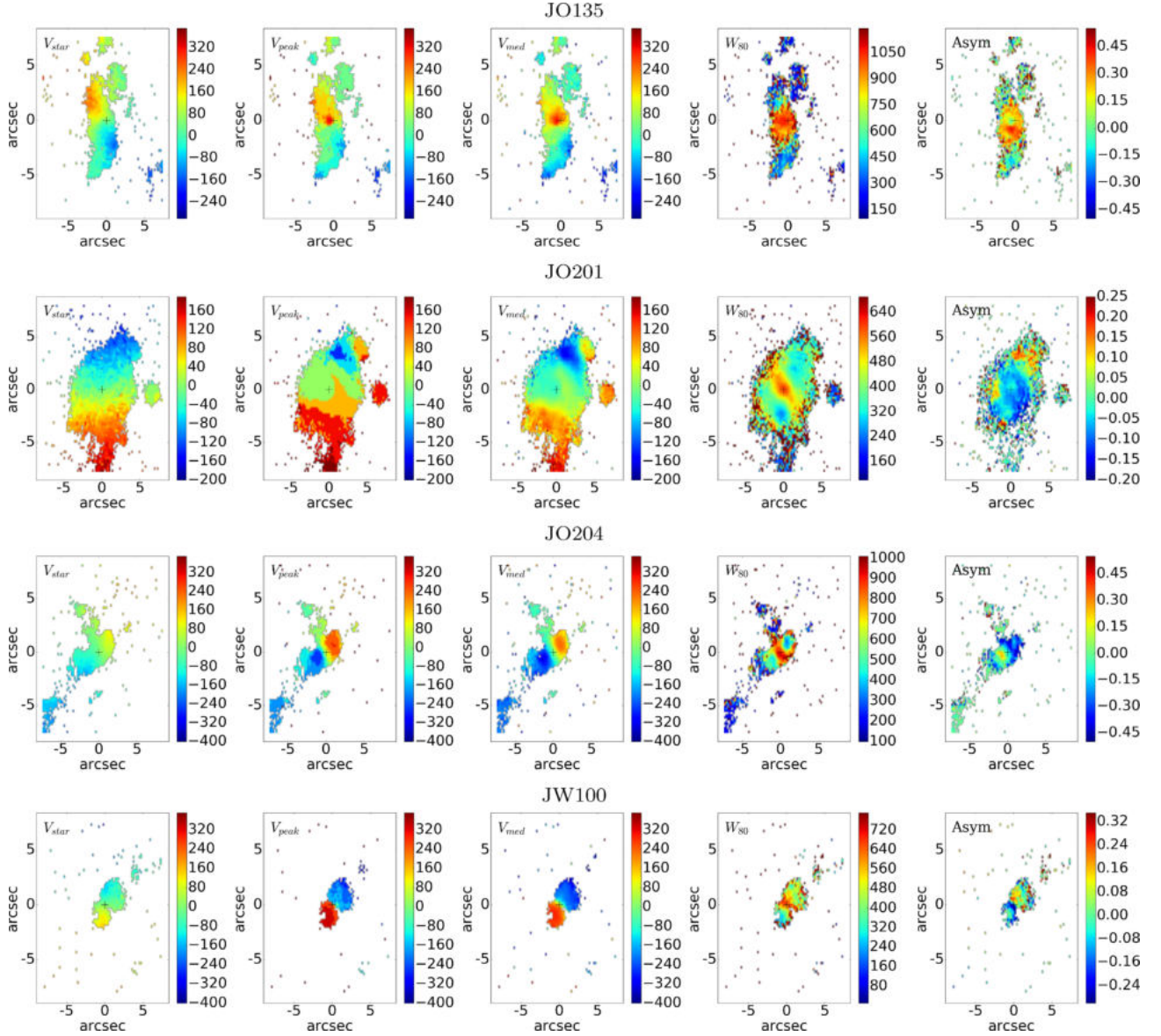
Figure 8. For each galaxy hosting an AGN, the plots display the spatial distribution of the stellar velocity (km s^{-1}) (*first panel*) and of the following parameters (see text for details) derived from the [O III] line: peak and median velocity (km s^{-1}); W_{80} (km s^{-1}); asymmetry (*right-hand panel*). In each plot, North is up and East is at left.

JO204: both the peak and median velocities differ from the stellar velocities (see also Gullieuszik et al. 2017) within a region of size ∼2 kpc. In a narrow central strip around the centre, emission line profiles are complex (see Fig. 2), thus producing higher values of W_{80} (∼900 km s^{-1}). Outside this strip, we identify two regions, one (NW) with blue asymmetric lines and one (SE) with red asymmetric lines. From the two-component fits, we find a narrow component, where σ_v is close to the stellar values, and a significantly broader, but fainter, one ($\sigma_v \leq 500$ km s^{-1}). Since up to a distance of 1 kpc both components have a velocity that is significantly different than the stellar value, we interpret both of them as produced by the two sides of a biconical outflow; at larger distances (>1 kpc) the gas is most likely dominated by the disc component.

JW100: we detect two line components, both of which are narrow ($\sigma_v < 200$ km s^{-1}), blue and redshifted, with a velocity

offset compared to the stellar velocity of $v \sim \pm 200$ km s^{-1} up to a radius $r \sim 2.5$ kpc. The two components are emitted from distinct regions, with the exception of a small area around the centre where a double-peaked profile is observed. As for JO204, we interpret this as a biconical outflow, extending to a distance of ∼2 kpc.

4.2 Outflow: size, mass, and energy

From the *secondary* (broader) components, we computed the radius containing a fraction f ($f = 50$ per cent and 90 per cent) of the total broad [O III] flux: $\sum_{r<r_f} F_{[O\,III],broad} = f \sum_{r<r_{max}} F_{[O\,III],broad}$, r_{max} being the outer radius where the presence of the second component is significant. We adopted r_{90} as the outflow size as it agrees with a dynamic definition of the outflow size (Karouzos et al. 2016a), that is the radius where the velocity and velocity dispersions of
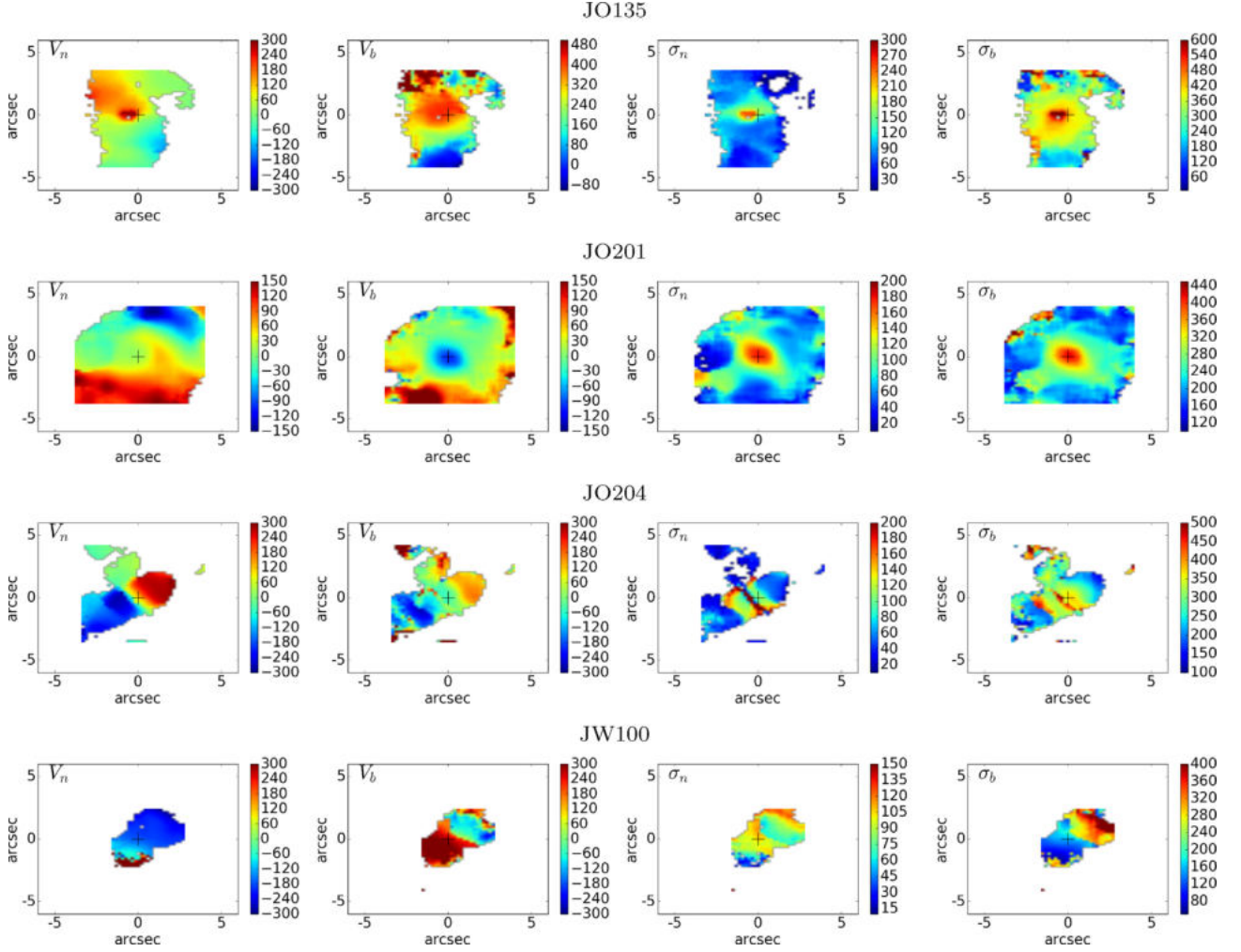
**Figure 9.** Spatial distribution of velocity and velocity dispersion from [O III] λ5007 for galaxies with two components.

the outflow component start to decline and approach the stellar values.

The mass related to the outflow is (Carniani et al. 2015) $M_{out} = 8 \times 10^7 M_\odot C \frac{L[O\,III]}{10^{44}\mathrm{ergs}^{-1}} \left(\frac{<n_e>}{500\,\mathrm{cm}^{-3}} \right)^{-1}$, with $C = \langle n_e \rangle^2 / \langle n_e^2 \rangle \sim 1$. A typical density $\langle n_e \rangle = 500$ cm $^{-3}$ was assumed. The outflow kinetic energy is $E_{kin} = \frac{1}{2} M_{out} v_{out}^2$, v_{out} being the bulk velocity of the outflow. As discussed in Karouzos, Woo & Bae (2016b), different choices to estimate v_{out} were made in the literature, reflecting different strategies to take into account geometrical effects (e.g. projection, opening angle of the outflow). Here we adopt the approximation (Karouzos et al. 2016b; Harrison et al. 2018) $v_{out}^2 = v_{rad}^2 + \sigma^2$, where v_{rad} is the measured radial velocity and σ the [O III] velocity dispersion, corrected (Karouzos et al. 2016b) for the contribution from the gravitational potential by subtracting in quadrature the stellar velocity dispersion. The mass outflow was derived summing on all spaxels within r_{90} the contributes from both line components since, with the possible exception of JO201, we were not able to unambiguously separate the disc and outflow contributions to [O III].

From the mean bulk velocity and the size of the outflow we can then compute the outflow lifetime, $t_{out} = r_{out}/\bar{v}_{out}$, the outflow mass rate, $\dot{M}_{out} = M_{out}/t_{out}$, the energetic rate, $\dot{E}_{kin} = E_{kin}/t_{out}$, and the outflow efficiency, $\eta = \dot{E}_{kin}/L_{AGN}$ where L_{AGN} is the bolometric luminosity. In Karouzos et al. (2016b) the bolometric AGN lumi-

nosity was computed as $L_{AGN} = 3500 L_{[O\,III]}$ erg s^{-1} (Heckman et al. 2004), $L_{[O\,III]}$ being the dust uncorrected luminosity, for comparison with other literature samples. We adopted the same choice and used the [O III] luminosities in Table 1, that include both emission line components.

The results obtained from the above analysis are displayed in Table 3. We emphasize all the uncertainties related both to the outflow kinetic energy and the estimate of the bolometric luminosity. Nevertheless, the outflow mass rates and kinetic energies that we obtain are comparable with the values obtained by Karouzos et al. (2016b) in a sample of AGN having similar [O III] luminosities ($L_{[O\,III]} < 10^{42}$ erg s^{-1}). Consistently with these results, we derive low efficiencies, $\eta \ll 0.01$ per cent, suggesting that the outflow is not able to impact the host galaxy environment on large scales. As discussed by Bing et al. (2019), moderate luminosity AGN may however suppress the star formation in the inner few kpc. For the galaxies in our sample, the outflow lifetime derived above is $t_{out} \sim 10^7$ yr and the outflow velocity is $v_{out} \sim 300$ km s^{-1}: this corresponds to a distance of ~3 kpc up to which the outflow can propagate from the centre, in agreement with the outflow size (r_{90} in Table 3). Evidence for star formation suppression around the AGN in JO201, based on NUV and CO data, will be presented in George et al. (in preparation). For comparison, from literature the mass outflow and energy rates in the brightest AGN ($L_{[O\,III]} > 10^{43}$ erg s^{-1}) can be
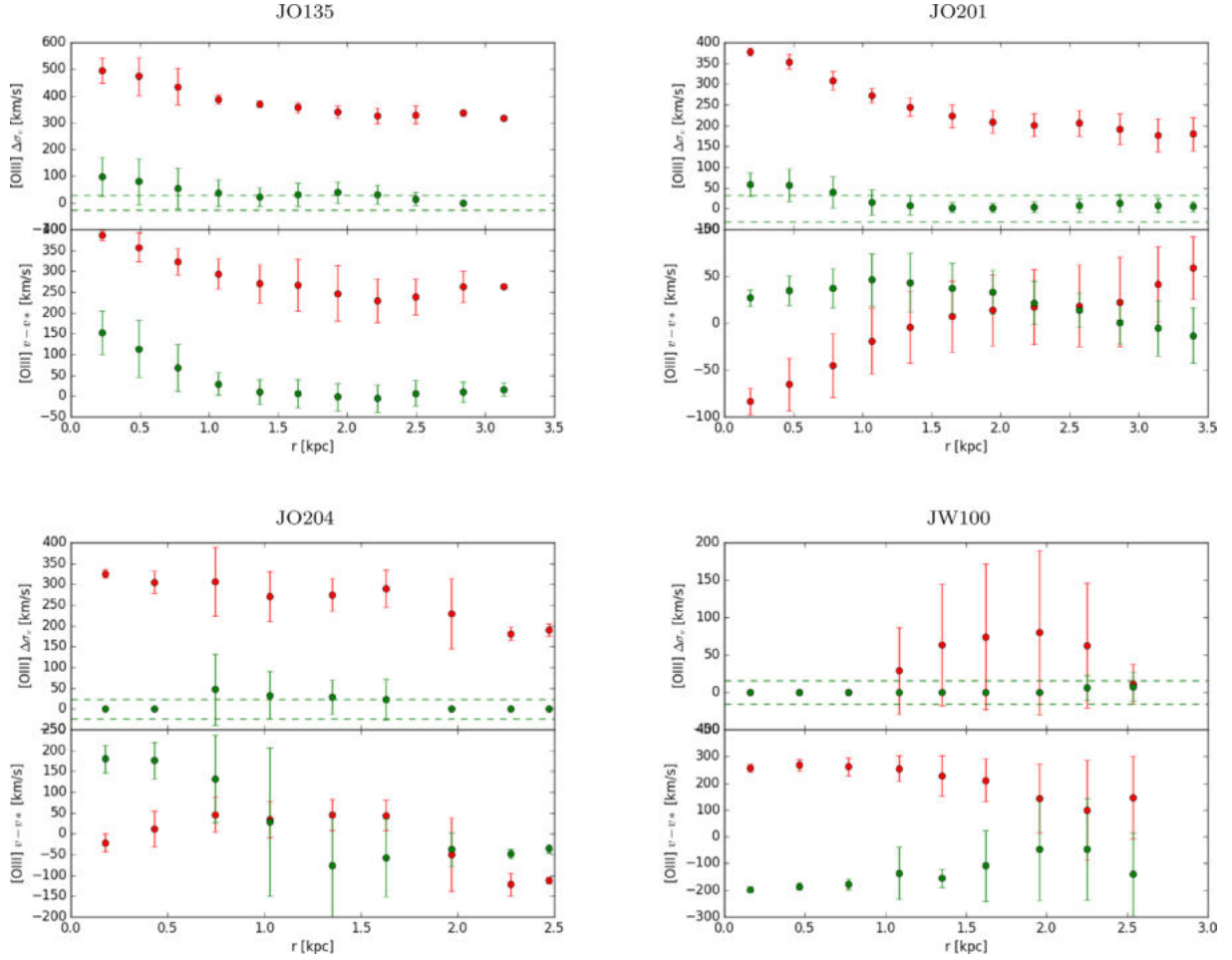
Figure 10. Velocity and velocity dispersion of the narrow (green) and broad (red) components of [O III] λ5007. The velocity of the stars is subtracted from the velocity, while $\Delta\sigma_v$ is the velocity dispersion from which the stellar velocity dispersion was subtracted in quadrature. For the velocity dispersion, a value of 0 was assigned if the velocity dispersion was lower than the stellar velocity dispersion.

Table 3. Outflow properties derived as described in the text.

Id	r_{50} (kpc)	r_{90} (kpc)	$\log E_{kin}$ (erg)	$\bar{v}_{out}$ (km s^{-1})	$\log t_{out}$ (yr)	$\log M_{out}$ (M$_\odot$)	$\log \dot{M}_{out}$ (M$_\odot$ yr^{-1})	$\log \dot{E}_{kin}$ (erg s^{-1})	$\log L_{AGN}$ (erg s^{-1})
JW100	1.1	2.1	50.5	248	6.9	4.40	−2.53	36.0	43.9
JO201	1.1	2.4	53.7	261	6.9	5.99	−0.95	39.2	45.4
JO204	0.7	1.2	52.2	317	6.6	4.27	−2.31	38.1	43.8
JO135	0.9	1.5	53.7	544	6.4	5.27	−1.16	39.7	44.8

as high as 10^4 M$_\odot$ yr^{-1} and $\dot{E}_{kin} \sim 10^{45}$ erg s^{-1} (Liu et al. 2013), thus being able to impact on much larger scales in the host galaxy environment.

5 CONCLUSIONS

In this paper we have carried out a detailed investigation of the seven jellyfish galaxies presented in P17b, where based on the [N II]/H α ratio it was found that at least five of them (JO201, JO204, JO206, JO135, and JW100) host an AGN. We first performed a detailed comparison with photoionization and shock model taking into account several diagnostic diagrams simultaneously. We concluded

that while shock models can play a role in the ionization of the gas, AGN models are required to explain the line ratios observed in the nuclear regions of these five galaxies: this conclusion is corroborated by an analysis of the H β luminosity. The presence of iron coronal lines in the nuclei of JO201 and JO135 indicates the existence of hot ($T \sim 10^5$ K) gas heated by the AGN. JO204 and JO135 also present EELR of >10 kpc that are ionized by the AGN. In JO194, that was classified as a LINER in P17b, line ratios in the central spaxels are better reproduced by an AGN model, though shock models may also marginally reproduce the observed ratios. Finally, in JO175 the [N II] λ6583/H α ratio is typical of star-forming regions, but we still observe a high [O I] λ6300/H α ratio that could point to the presence of shocks.

We then focused on the [O III] $\lambda5007$ line profile, which is a good tracer of the presence of outflowing gas. Four of the galaxies hosting an AGN present complex emission line profiles, with at least two Gaussian components with different line widths that testify the presence of AGN outflows. We have studied the properties and energetics of the outflows, with results comparable to what reported in other AGN of similar luminosity ($L_{[O III]} < 10^{42}$ erg s^{-1}), with outflows. Finally, we derived conclusions on possible AGN feedback effects on the circumnuclear regions ($\sim$3 kpc).

This study confirms on much more solid ground the conclusions from P17b regarding the presence of an AGN in several GASP jellyfish galaxies with the longest tails, that suggests a causal connection between ram pressure stripping and AGN activity. Moreover, in this work we demonstrate the presence of outflows and derive their properties. The current sample is too small to draw final conclusions regarding the AGN-ram pressure connection, and a detailed analysis of the whole GASP sample will be presented in a forthcoming paper, investigating the evidence for AGN activity in the other jellyfish galaxies with long tails but also for different stripping stages and as a function of the galaxy mass.

REFERENCES

Allen M. G., Groves B. A., Dopita M. A., Sutherland R. S., Kewley L. J., 2008, ApJS, 178, 20

Arnold T. J., Martini P., Mulchaey J. S., Berti A., Jeltema T. E., 2009, ApJ, 707, 1691

Bacon R. et al., 2010, in McLean I. S., Ramsay S. K., Takami H., eds, Proc. SPIE Conf. Ser. Vol. 7735, Ground-based and Airborne Instrumentation for Astronomy III. SPIE, Bellingham, p. 773508

Bae H.-J., Woo J.-H., 2014, ApJ, 795, 30

Bae H.-J., Woo J.-H., Karouzos M., Gallo E., Flohic H., Shen Y., Yoon S.-J., 2017, ApJ, 837, 91

Balmaverde B. et al., 2016, A&A, 585, A148

Belfiore F. et al., 2016, MNRAS, 461, 3111

Bellhouse C. et al., 2017, ApJ, 844, 49

Bing L. et al., 2019, MNRAS, 482, 194

Cappellari M., Emsellem E., 2004, PASP, 116, 138

Carniani S. et al., 2015, A&A, 580, A102

Crenshaw D. M., Schmitt H. R., Kraemer S. B., Mushotzky R. F., Dunn J. P., 2010, ApJ, 708, 419

Davies R. L. et al., 2016, ApJ, 824, 50

Davis T. A. et al., 2012, MNRAS, 426, 1574

Dopita M. A., Sutherland R. S., 1995, ApJ, 455, 468

Dressler A., Thompson I. B., Shectman S. A., 1985, ApJ, 288, 481

Ebeling H., Stephenson L. N., Edge A. C., 2014, ApJ, 781, L40

Ehlert S. et al., 2014, MNRAS, 437, 1942

Fabian A. C., 2012, ARA&A, 50, 455

Ferguson J. W., Korista K. T., Baldwin J. A., Ferland G. J., 1997, ApJ, 487, 122

Fossati M., Fumagalli M., Boselli A., Gavazzi G., Sun M., Wilman D. J., 2016, MNRAS, 455, 2028

Fritz J. et al., 2017, ApJ, 848, 132

Fu H., Stockton A., 2009, ApJ, 690, 953

Fumagalli M., Fossati M., Hau G. K. T., Gavazzi G., Bower R., Sun M., Boselli A., 2014, MNRAS, 445, 4335

George K. et al., 2018, MNRAS, 479, 4126

Gitti M., 2013, MNRAS, 436, L84

Gullieuszik M. et al., 2017, ApJ, 846, 27

Harrison C. M., Alexander D. M., Mullaney J. R., Swinbank A. M., 2014, MNRAS, 441, 3306

Harrison C. M., Costa T., Tadhunter C. N., Flütsch A., Kakkad D., Perna M., Vietri G., 2018, Nat. Astron., 2, 198

Heckman T. M., Best P. N., 2014, ARA&A, 52, 589

Heckman T. M., Kauffmann G., Brinchmann J., Charlot S., Tremonti C., White S. D. M., 2004, ApJ, 613, 109

Ilha G. S. et al., 2019, MNRAS, 484, 252

Jaffé Y. L. et al., 2018, MNRAS, 476, 4753

Kakkad D. et al., 2018, A&A, 618, A6

Karouzos M., Woo J.-H., Bae H.-J., 2016a, ApJ, 819, 148

Karouzos M., Woo J.-H., Bae H.-J., 2016b, ApJ, 833, 171

Kewley L. J., Groves B., Kauffmann G., Heckman T., 2006, MNRAS, 372, 961

Komossa S., Schulz H., 1997, A&A, 323, 31

Korista K. T., Ferland G. J., 1989, ApJ, 343, 678

Krumholz M. R., Fumagalli M., da Silva R. L., Rendahl T., Parra J., 2015, MNRAS, 452, 1447

Lena D. et al., 2015, ApJ, 806, 84

Liu G., Zakamska N. L., Greene J. E., Nesvadba N. P. H., Liu X., 2013, MNRAS, 436, 2576

Maddox N., 2018, MNRAS, 480, 5203

Marshall M. A., Shabala S. S., Krause M. G. H., Pimbblet K. A., Croton D. J., Owers M. S., 2018, MNRAS, 474, 3615

Marziani P. et al., 2017, A&A, 599, A83

Mazzalay X., Rodríguez-Ardila A., Komossa S., 2010, MNRAS, 405, 1315

Mingozzi M. et al., 2019, A&A, 622, A146

Nevin R., Comerford J., Müller-Sánchez F., Barrows R., Cooper M., 2016, ApJ, 832, 67

Osterbrock D. E., Ferland G. J., 2006, Astrophysics of gaseous nebulae and active galactic nuclei, University Science Books, Ferland. Sausalito, CA

Pimbblet K. A., Shabala S. S., Haines C. P., Fraser- McKelvie A., Floyd D. J. E., 2013, MNRAS, 429, 1827

Poggianti B. M. et al., 2017a, ApJ, 844, 48 (P17a)

Poggianti B. M. et al., 2017b, Nature, 548, 304 (P17b)

Poggianti B. M. et al., 2019, MNRAS, 482, 4466

Proxauf B., Öttl S., Kimeswenger S., 2014, A&A, 561, A10

Ramos-Martínez M., Gómez G. C., Pérez-Villegas Á., 2018, MNRAS, 476, 3781

Rawle T. D. et al., 2014, MNRAS, 442, 196

Smith R. J. et al., 2010, MNRAS, 408, 1417

Thomas A. D., Groves B. A., Sutherland R. S., Dopita M. A., Kewley L. J., Jin C., 2016, ApJ, 833, 266

Thomas A. D. et al., 2017, ApJS, 232, 11

Thomas A. D., Dopita M. A., Kewley L. J., Groves B. A., Sutherland R. S., Hopkins A. M., Blanc G. A., 2018, ApJ, 856, 89

Vazdekis A., Sánchez-Blázquez P., Falcón-Barroso J., Cenarro A. J., Beasley M. A., Cardiel N., Gorgas J., Peletier R. F., 2010, MNRAS, 404, 1639

Veilleux S., Osterbrock D. E., 1987, ApJS, 63, 295

Venturi G. et al., 2018, A&A, 619, A74

Whittle M., 1985, MNRAS, 213, 1

Wong K.-W., Sarazin C. L., Blanton E. L., Reiprich T. H., 2008, ApJ, 682, 155

Woo J.-H., Bae H.-J., Son D., Karouzos M., 2016, ApJ, 817, 108

Yoshida M. et al., 2004, AJ, 127, 90

This paper has been typeset from a TeX/LaTeX file prepared by the author.